ORIGINAL RESEARCH ARTICLE

Effect of Boron Addition on the Microstructure, Thermal, and Mechanical Properties of Al-5%Mg-2%Ti Alloy

Hakan Yaykaşlı[1,2] · Musa Göğebakan[3]

Abstract

In this study, $Al_{93-x}Mg_5Ti_2B_x$ ($x = 1,2,3,4\%$) quaternary alloys are produced by casting techniques. The microstructure properties of the alloys were performed by x-ray diffraction (XRD), scanning electron microscopy (SEM), and energy dispersive x-ray spectroscopy (EDS) analysis. Differential scanning calorimetry (DSC) investigated the alloys' thermal properties. The mechanical properties of alloys were performed by Vickers microhardness and tensile tests. In addition, tensile tests were performed on alloys, and SEM images of the rupture surface were obtained. The XRD analysis results of the alloys produced α-Al, β-Al_3Mg_2, $Al_{12}Mg_{17}$, Al_3Ti, and AlB_2 phases were observed. SEM and EDS analysis of the alloys showed that the distribution of the phases was homogeneous. It was determined that, adding boron to the ingot alloys caused an increase in the Vickers microhardness value and tensile strength of the alloy. Tensile test fracture surface SEM images showed a brittle and brittle fracture appearance.

Keywords Aluminum alloys · Casting methods · Mechanical properties · Microstructure

Introduction

Aluminum-based alloys of superior properties operate broadly in many industry areas. Mainly, light alloys, the improvement of their properties, and the reduction of production costs attract the attention of researchers [1, 2]. Light-weight aluminum-based alloys are necessary for energy-saving and fuel efficiency in the aerospace and industry sectors. Alloys consisting of elements with low densities are named light alloys, such as Al (2.70 g/cm³), Mg (1.74 g/cm³), Si (2.33 g/cm³), and B (2.47 g/cm³). These alloys are widely preferred in applications due to their low specific gravity, high specific strength, corrosion resistance, and easy formability [3–5]. Besides, Al-alloy's workability and

mechanical properties stand out from the alloy's intermetallic microstructure [6]. It has been seen that these alloys have the potential for industrial applications [7].

Al-based alloys have been determined that the alloys formed with the addition of titanium boride to the Mg-Al-Ti-B quaternary alloy reached high yield and tensile strength. The material created by doping titanium boride to the Mg-Al-Ti-B quaternary alloy has been determined to provide high yield and tensile strength [8]. Gras et al. have reported a detailed study of micro-defect formation in the production of aluminum alloys [9]. The elements and the ratio that make up the alloys are the most critical factors affecting the properties of the alloy. Mg, Si, Ti, Zn, and Cu are commonly preferred in Al-based light alloys [10]. The microstructure of Al-based alloys consists of single or multiple intermetallic phases [11, 12]. Besides, in Al-Mg alloys, intermetallic phases like β-Al_3Mg_2 and Al_3Ti are primarily found, making them easy for intergranular cracking [13, 14]. The homogeneous distribution of the intermetallic phases throughout the material positively affects many properties, especially mechanical ones [15]. Techniques such as rapid solidification, mechanical alloying, arc melting, and normal solidification (casting) are preferred in light alloy production [16]. Heat treatment techniques are among the most noteworthy developments in Al-based alloys. Heat treatment of alloys

✉ Hakan Yaykaşlı
  hakan.yaykasli@istiklal.edu.tr

1 Department of Property Protection and Safety, Elbistan Vocational School of Higher Education, Kahramanmaraş İstiklal University, Kahramanmaraş, Turkey

2 Department of Material Science and Engineering, Institute of Graduate Studies, Kahramanmaraş İstiklal University, Kahramanmaraş, Turkey

3 Department of Physics, Faculty of Science, Kahramanmaraş Sütçü İmam University, Kahramanmaraş, Turkey

can improve or eliminate casting defects such as segregation, undesirable stresses, and inhomogeneous microstructure [17, 18]. Although there are many studies on Al-based alloys, there are no studies on Al-Mg-Ti-B alloys.

In this study, using the normal solidification technique, the impact of different concentrations of boron on the microstructure, mechanical, and thermal properties of Al-Mg-Ti-B$_x$(x = 1,2,3,4%) alloy production. The microstructures were analyzed with the aid of x-ray diffraction (XRD), x-ray fluorescence (XRF), energy dispersive x-ray (EDS), and scanning electron microscopy (SEM). Tensile and Vickers microhardness tests investigated mechanical properties.

Experimental

This study used the normal solidification technique to produce the Al$_{93-x}$Mg$_5$Ti$_2$B$_x$(x = 1,2,3,4%) alloys as ingots. The compositions of these alloys are given in Table 1. The starting metals Aluminum (Al), Magnesium (Mg), Titanium (Ti), and Boron (B), with a purity of 99%, were supplied by Merck Company. Alloys were melted in a graphite crucible with an MTI-SP-15A portable high-frequency induction heater. High-purity argon gas was used to control the alloy from oxidizing during the melting operation. Magnesium element was added when the melt temperature of the alloy was at 750 °C. The melt temperature was measured with the CEM DT 8869H dual laser remote thermometer at each stage. The molten alloy was cast into the metal mold at room temperature. Ingot alloys were obtained by cooling under room temperature conditions. All alloys were produced under the same conditions. Alloys were heat-treated at 100 °C, 200 °C, 300 °C, 400 °C, and 500 °C for 2 hours in the atmospheric environment.

Metallographic preparatory operations have been carried out to examine the structural and mechanical properties of the alloys. Alloys were cut with a Struers Minitom brand precision cutting device, and the samples were brought to inspectable dimensions. Then, the surfaces of the alloys were polished with polishing cloths after rough and fine sanding processes by mounting Metkon brand DMT-CON conductive acrylic cold molding. The ZEISS EVO LS10 scanning

electron microscope (SEM) investigated the morphology of ingot alloys. Energy dispersive x-ray spectrometry (EDS) and wavelength dispersive x-ray fluorescence spectrometry (WXRF) were used for the quantitative, qualitative elemental analyzes of the as-cast samples. Philips X'pert Pro x-ray diffraction (XRD) was utilized to identify phases formed within the alloys. The thermal properties of the alloys were analyzed with Perkin-Elmer Sapphire differential scanning calorimetry (DSC), and the analysis conditions were heated at 50 °C/min from 300 °C to 700 °C in a Nitrogen atmosphere. The tensile test was exerted according to ASTM: E8-04 standards on a Zwick Roell 100 kN Model tensile machine at a strain rate of 1 s^{-1}. The ingot alloys employed Vickers microhardness tests (Shimadzu HMV-2) with a 298 K de 9.807 N (HV1) load. Vickers microhardness results were calculated with the following equation (1).

$$HV = \frac{1.854(P)}{d^2} \tag{1}$$

Here, P is the load, d is the diagonal length of the trace formed by the load, and θ = 136º is the angle between the opposite surfaces of the diamond tip. The average microhardness values have been taken from 10 different regions of measurement.

Results and Discussion

Microstructural Characterizations

XRD Analysis

XRD graphs of the starting elements of Al$_{93-x}$Mg$_5$Ti$_2$B$_x$(x = 1,2,3,4%) are given in Figure 1. The XRD analysis of starting elements observed characteristic phase peaks of pure elements. ICDD reference codes have been determined for elements Al (00-001-1180), Mg (00-035-0821), Ti (00-044-1294), and B (01-085-0409). It is seen that all initial elements are in the crystalline structure. Microstructure and phases of alloys produced by normal solidification were determined with X'Pert High Score software and the ICDD-PDF 2 library and compared with the literature.

Figure 2 shows the result of the XRD graph of the phases formed and changed with the increase in the boron ratio (1%, 2%, 3%, and 4%). Peaks belonging to the phases of the alloys were detected of α-Al in (ICDD Card No: 01-089- 2837) cubic, β-Al$_3$Mg$_2$ (ICDD Card No:00-001-1132) hexagonal, Al$_{12}$Mg$_{17}$ (ICDD Card No:01-073-1148) cubic, Al3Ti (ICDD Card No:03-065-4694) tetragonal, and AlB$_2$ (ICDD Card No:00-009-0154) hexagonal structures. The formation of the same phases in alloys means that the microstructures

Table 1 Nominal chemical composition of the Al-Mg-Ti-B alloys (wt.%)

Composition of alloy	Element [wt.%]			
	Al	Mg	Ti	B
Al$_{92}$Mg$_5$Ti$_2$B$_1$	92.0	5.0	2.0	1.0
Al$_{91}$Mg$_5$Ti$_2$B$_2$	91.0	5.0	2.0	2.0
Al$_{90}$Mg$_5$Ti$_2$B$_3$	90.0	5.0	2.0	3.0
Al$_{89}$Mg$_5$Ti$_2$B$_4$	89.0	5.0	2.0	4.0
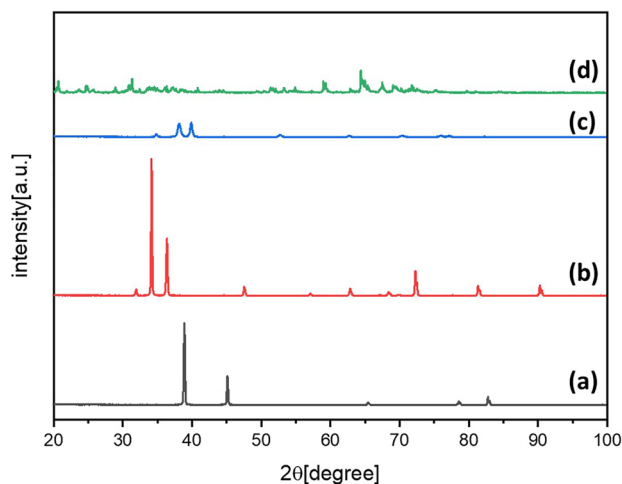
Fig. 1 The XRD patterns for starting elements of alloys: **a** Al, **b** Mg, **c** Ti, and **d** B
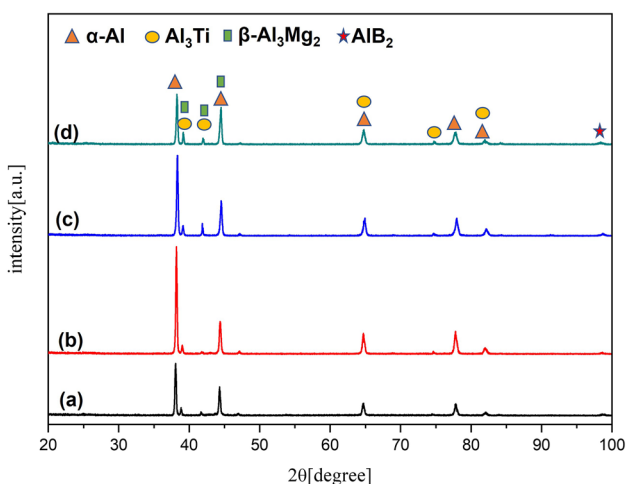
Fig. 2 The XRD patterns for alloys: **a** $Al_{92}Mg_5Ti_2B_1$, **b** $Al_{91}Mg_5Ti_2B_2$, **c** $Al_{90}Mg_5Ti_2B_3$, and **d** $Al_{89}Mg_5Ti_2B_4$

of all alloys are the same. The absence of reflected peaks from pure Mg, Ti, and B elements is due to the reaction of these elements with other elements to form compounds. In addition, as shown in Figure 2, the peaks reflected from the α-Al phase are the most intense among these phases. This is because the Al content in the alloy is the highest. The represent the phases forming the microstructure of the alloy $2\theta = 38°, 41°, 44°, 47°, 65°, 74°, 77°, 82°,$ and $98°$ peaks. The α-Al phase observed in alloys differs from the pure Al phase and contains a certain amount of B, Mg, and Ti. In some cases, the α-Al phase can also be expressed as α-Al (Mg, Ti, B). There are similar results in the literature [19, 20]. At the same time, the reflection of the most substantial peak from the α-Al phase in the XRD results shows that the volume ratio of the α-Al phase in the alloy's microstructure

is the largest. The β-Al_3Mg_2, $Al_{12}Mg_{17}$, Al_3Ti, and AlB_2 intermetallic phases observed in the microstructures of the alloys are in a crystalline structure, and these phases are in harmony with the Al and Mg, Ti, and B binary phase diagrams [21, 22]. The ratios of Mg and Ti are constant in alloys, and the boron concentration increases with the decrease in the Al ratio. This increase causes a slight reduction in the intensity of the peaks of the α-Al phase. This decrease is because element B (atomic radius) with a smaller atomic radius is dissolved in Al (atomic radius). The increase in the ratio of boron element in Al causes the expansion of the lattice structure of the fcc-Al phase. In addition, increasing the B ratio did not cause any new boron-containing peak formation but caused a relative increase in the intensity of the AlB_2 intermetallic phase. Boron element combines with Al to form an intermetallic aluminum boride phase like AlB_2. This phase is important in the microstructure of the materials, showing grain refinement and affecting the material's mechanical properties mainly. Magnesium is often used in aluminum-based alloys to increase hardness and ductility. The literature has determined that adding titanium to the high-strength Al-Si alloy (0.1%, 1, 2, 3, 5, and 10%) increases the mechanical strength after heat treatment [23]. In the production of alloys, the solidification rate ensures that the phases are formed dimensionally uniformly. It causes an increase in the size of the intermetallic phases at low solidification rates. A similar study in the literature stated that the aluminum ratio is generally high in microstructures in which intermetallic phases occur, according to XRD results [11].

SEM and EDS Analysis

Figure 3 shows SEM images of the alloys produced by normal solidification. As seen in the SEM photographs of these alloys, the most prominent phase in the microstructure is the white rod-like structures. In addition, there are dark-colored base areas, gray-colored dendritic structures, and very few point-like or small fracture structures. These structures in the SEM photograph correspond to different phases, which agrees with the XRD results. Figure 4 shows the EDS mapping of the alloys produced by normal solidification. According to these results, it was seen that the composition of the alloy made was compatible with the initial composition, and the distribution was homogeneous. EDS analyzes have determined that the dark-colored primary area in the microstructure of the alloys to the α-Al phase, the white rod-like structures to the Al_3Ti phase, and the gray-colored structure in the β-Al_3Mg_2, $Al_{12}Mg_{17}$ phases and the point-like small fracture structures the AlB_2 phases. The alloy morphology consists of rod-like structures, indicating that the solidification rate is high and unidirectional. A previous study detected
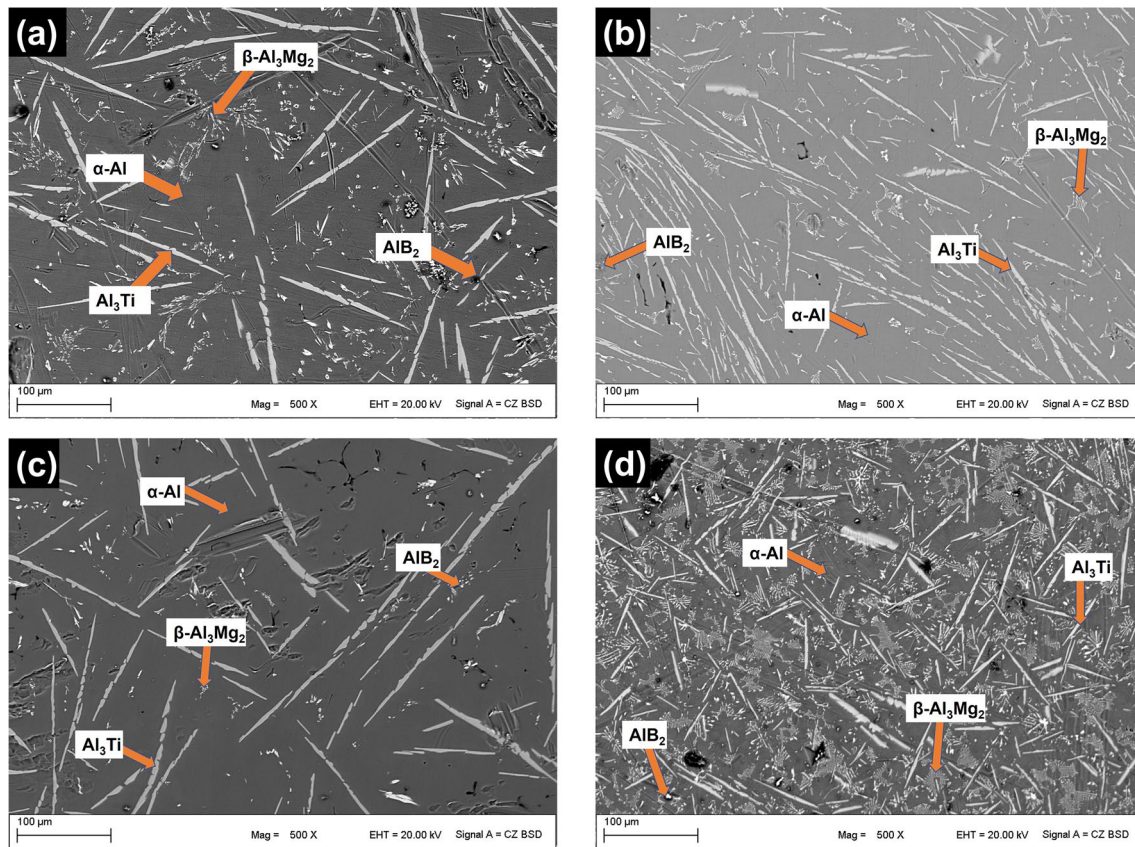
Fig. 3 Typical SEM images for alloys: **a** $Al_{92}Mg_5Ti_2B_1$, **b** $Al_{91}Mg_5Ti_2B_2$, **c** $Al_{90}Mg_5Ti_2B_3$, and **d** $Al_{89}Mg_5Ti_2B_4$

rod-like phases in Al-Mg-Ti alloys produced by a similar method [11]. On the other hand, the particles forming the morphological structure of the $Al_{89}Mg_5Ti_2B_4$ alloy are smaller than the particles in the $Al_{92}Mg_5Ti_2B_1$ alloy. This result is thought to be caused by the decrease in the grain size of the alloy and the increase in the boron ratio. These results confirmed that the rise in the boron ratio causes a grain refinement effect in the alloy's microstructure. The results obtained in this study are similar to previous studies [24]. On the other hand, ingot alloys produced by normal solidification form porosity structures between grain boundaries. This is thought to be due to the different melting temperatures of the elements forming the alloy and the solidification of the alloy by cooling in the metal mold at room temperature. The voids formed on the surface of the alloy cause the material to be brittle and cause dislocations in the material, which is defined as a crystal defect. Xu-Guang An et al. reported similar results in their study [25]. The brittle fracture occurred in the tensile test results of these alloys. It is caused by the measured (porosity) structures detected in the SEM results and is compatible with pulling the test.

Quantitative Evaluation

XRF Analysis

XRF analysis was performed to verify the alloy's qualitative and quantitative elemental composition after the production of the elemental composition, which was calculated nominally according to the atomic concentrations of the starting elements of the alloys produced by normal solidification. Production is challenging since the densities of the elements that make up this alloy are low, and their melting temperatures are different from each other. Elemental loss after producing alloys of elements with different melting temperatures is expected. The XRF results of the alloys are given in Table 2. As the XRF results were examined, Al, Mg, and Ti elements forming the alloy could be detected. B element could not be seen in XRF analysis. This is because the Bruker S8 Tiger XRF spectroscopy analyzer has Quant Express semi-quantitative general analysis method, and the amount of B is low in the alloy. It is seen that the atomic compositions of the elements that make up the alloy are approximately similar by experimental calculation.
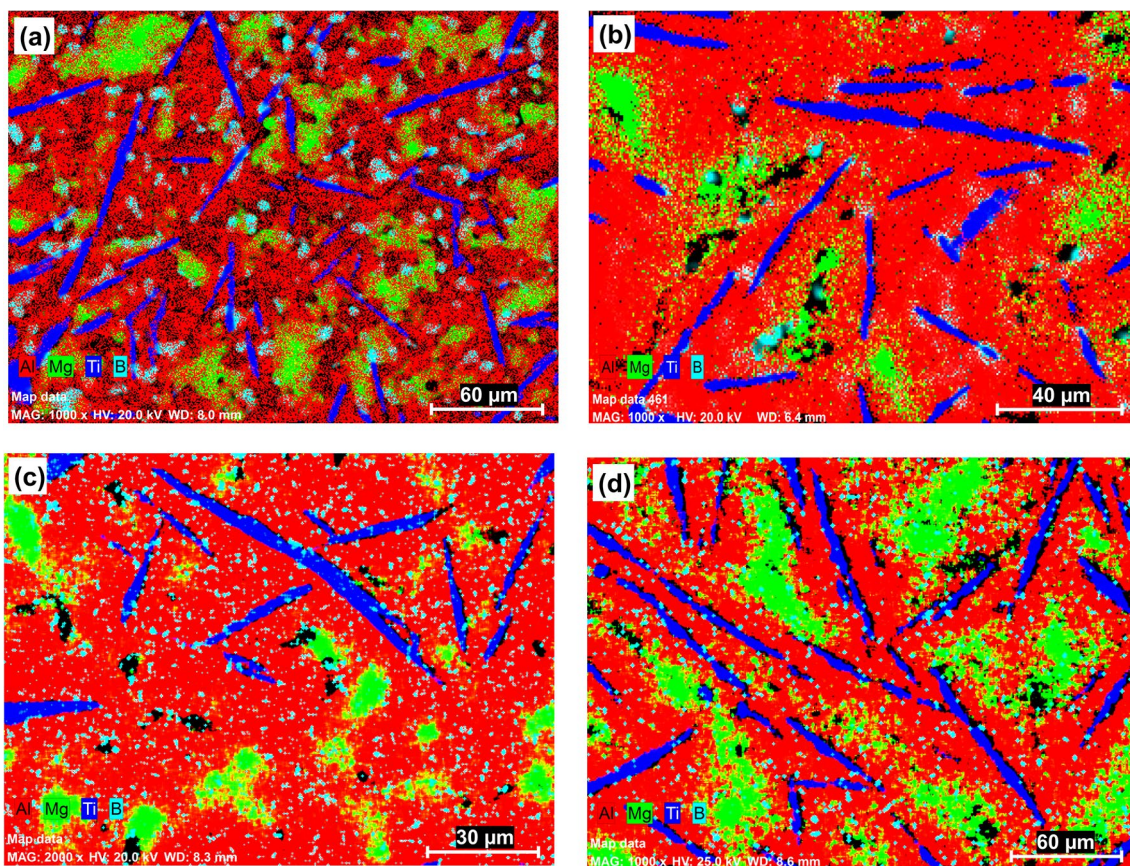
Fig. 4 EDS mapping analysis results of alloys: **a** $Al_{92}Mg_5Ti_2B_1$, **b** $Al_{91}Mg_5Ti_2B_2$, **c** $Al_{90}Mg_5Ti_2B_3$, and **d** $Al_{89}Mg_5Ti_2B_4$

**Table 2** WXRF analysis results of alloys the Al-Mg-Ti-B alloys of chemical composition

	Composition (at.%)			
Elements	$Al_{92}Mg_5Ti_2B_1$	$Al_{91}Mg_5Ti_2B_2$	$Al_{90}Mg_5Ti_2B_3$	$Al_{89}Mg_5Ti_2B_4$
Al	90.12	89.66	90.71	89.84
Mg	5.74	5.41	5.06	5.31
Ti	4.14	4.93	4.23	4.85

Heat Properties

DSC Analysis

Figure 5 shows the DSC thermal behavior of the alloys. An endothermic peak was observed only at 660 °C in the DSC analysis results of the alloys. No endothermic or exothermic peaks representing crystallization, glass transition, and phase transformation were observed. The endothermic peak observed at 660 °C corresponds to the melting temperature of aluminum. This is an expected result due to the high Al content in the alloy and the α-Al phase observed in the microstructure. When the DSC analysis results were examined, no peaks were observed that were reflected from other elements forming the alloy or represented intermetallic phases such as Al_3Ti, β-Al_3Mg_2, $Al_{12}Mg_{17}$, and AlB_2, which included the microstructure of the alloy. This is because the melting temperature of the intermetallic phases forming the alloy's microstructure is higher than 700 °C. On the other hand, with the increase in boron ratio in the alloy, it has been determined that there is a gradual decrease in the intensities of the endothermic peaks, which are observed around 660 °C and correspond to the melting of the α-Al phase. This is thought to be the increase in the volumetric ratio of the AlB_2 phase in the microstructure in the α-Al phase with the increase in the B ratio. In addition, the thermal stability of the obtained alloy up to 660 °C is essential for industrial use.
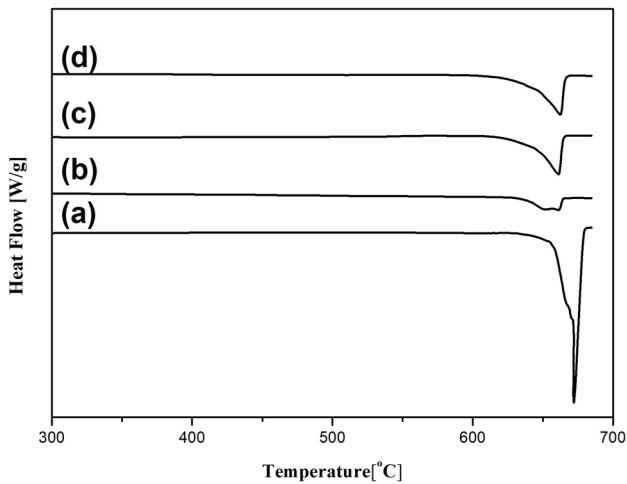
Fig. 5 DSC spectrum of alloys: **a** $Al_{92}Mg_5Ti_2B_1$, **b** $Al_{91}Mg_5Ti_2B_2$, **c** $Al_{90}Mg_5Ti_2B_3$, and **d** $Al_{89}Mg_5Ti_2B_4$

Mechanical Evaluations

Microhardness

One of the aims of this study is to produce light alloys as ingots and improve their mechanical properties. A load was applied to the surface to measure the Vickers microhardness value, and the microhardness value was calculated by measuring the trace created by this load on the surface. The average value was calculated by taking measurements from 10 different points. As shown in Figure 6, the microhardness values of the alloys $Al_{92}Mg_5Ti_2B_1$, $Al_{91}Mg_5Ti_2B_2$, $Al_{90}Mg_5Ti_2B_3$, and $Al_{89}Mg_5Ti_2B_4$, respectively; it was calculated as 122.8 ± 5 HV, 130.2 ± 11 HV, 133.9 ± 8 HV, and 134.6 ± 13 HV. Among these quaternary alloys obtained, the
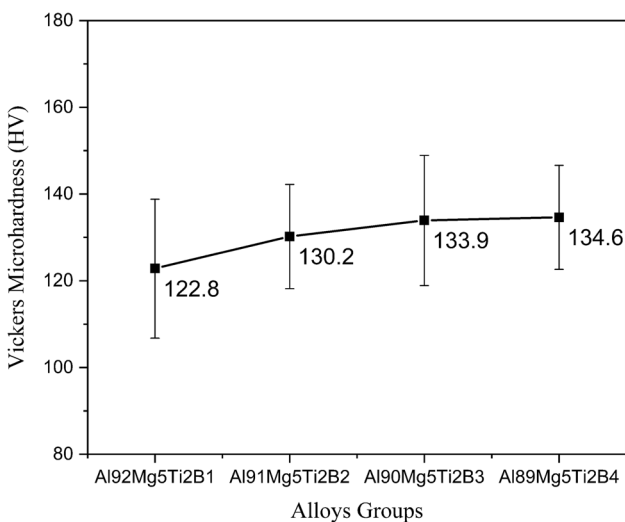
microhardness values of the $Al_{89}Mg_5Ti_2B_4$ alloy are higher than the microhardness values of the other alloys. According to these results, the increase in the boron ratio in the alloy increased the microhardness value of the alloy. It seems to be effects such as the grain refinement of the boron element and the crystal size reduction and phases. With the decrease in crystal size with the increase in boron, the microhardness value of the material increased. In addition, among the factors that increase the microhardness of the alloys, there are also factors such as plastic deformation hardening caused by heat loss during the solidification of the alloy and solid solution hardening caused by the atoms dissolved in the alloy. Such factors prevent dislocation movements and make the material harder [5]. The grain refiner property of boron has also been reported in a previous study [26]. On the other hand, it is known that there are significant changes in the mechanical properties of the material with the evolution of the microstructure of the materials [27–29].

Tensile Property and Fractography

A tensile test was carried out in more detail to examine the mechanical properties of alloys produced by normal solidification. Figure 7 demonstrates tensile test results. The tensile test of the samples prepared according to ASTM E8-04 standard conditions was performed at room temperature. The alloys' maximum tensile strength and percentage elongation value were calculated in the tensile test. As shown in Figure 7, the tensile strength of group A alloys reached a maximum value of 169.03 MPa when the boron ratio was increased to 2%. It was observed that this value decreased when the B ratio was 3% and 4%. The microstructure change during the solidification phase of the alloys produced by normal solidification is the parameter that affects the mechanical properties. It was observed that the highest percentage
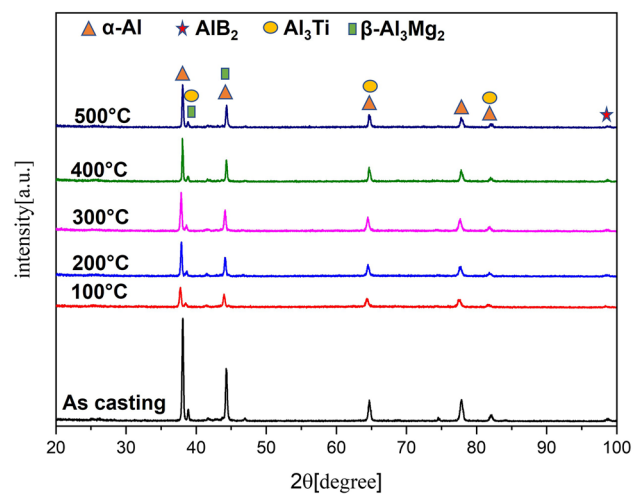

Fig. 6 Vickers microhardness values of alloys
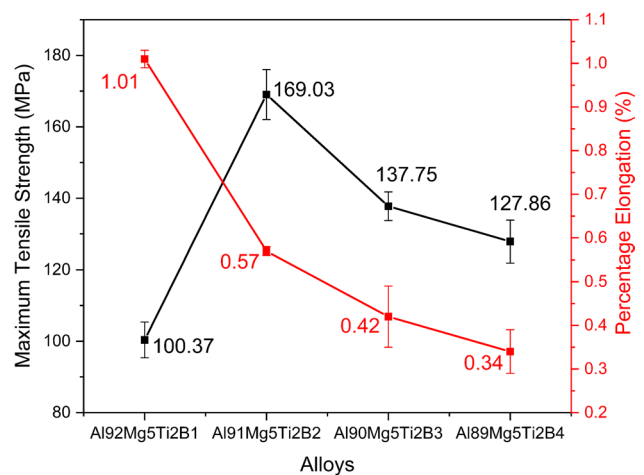
Fig. 7 Tensile Test Results of Alloys
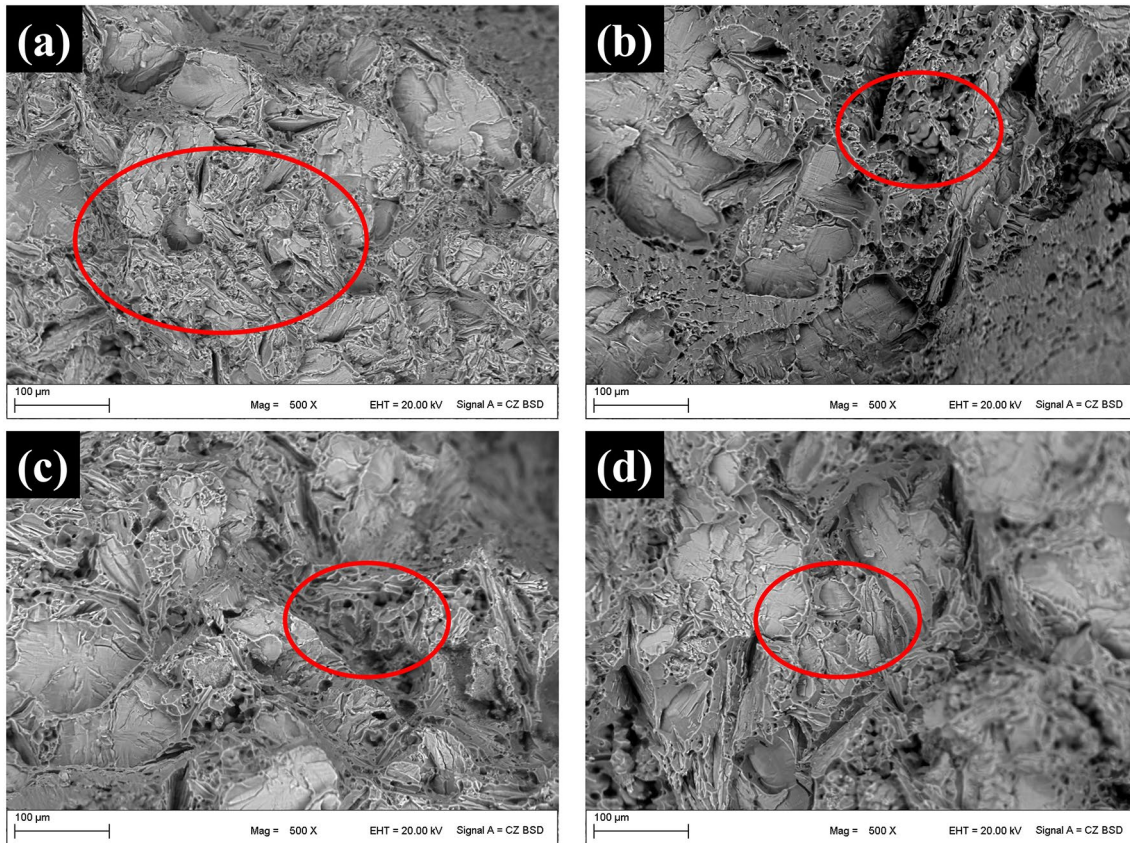
Fig. 8 After tensile tests of alloys, fracture surface SEM images **a** $Al_{92}Mg_5Ti_2B_1$, **b** $Al_{91}Mg_5Ti_2B_2$, **c** $Al_{90}Mg_5Ti_2B_3$, and **d** $Al_{89}Mg_5Ti_2B_4$

elongation (%) was 1.01 in the alloy, with the highest boron rate of 1%. It is seen that the percent elongation in the alloy with a boron content of 4% is 0.34. As a result, increasing the boron content increases the strength and decreases the amount of elongation.

As a result of the tensile test, the structure of the rupture regions of the samples was examined by taking SEM images. Figure 8 shows the micrographs of the fracture surfaces marked. As shown in Figure 8a, sharp surfaces and small dimples can be observed in a region marked. Intergranular fracture patterns exist in some areas, marked in Figure 8b, c, and d. In Figure 8d, many pits at different depths are observed, indicating that a ductile fracture has occurred in these regions and indicates brittle fracture on sharp surfaces [30]. Likewise, it was determined in the scanning electron microscope images taken from the rupture surface in the tensile test of the alloys in which the dendritic structure was formed in these alloys (Fig. 3). In similar studies; it was stated that the elongation in the dendritic structure caused a decrease in the tensile strength values [31–33]. The reason for this is thought to be because the boron element reaches its maximum solubility and forms a precipitate. When the rupture images of the rupture regions at the grain boundaries

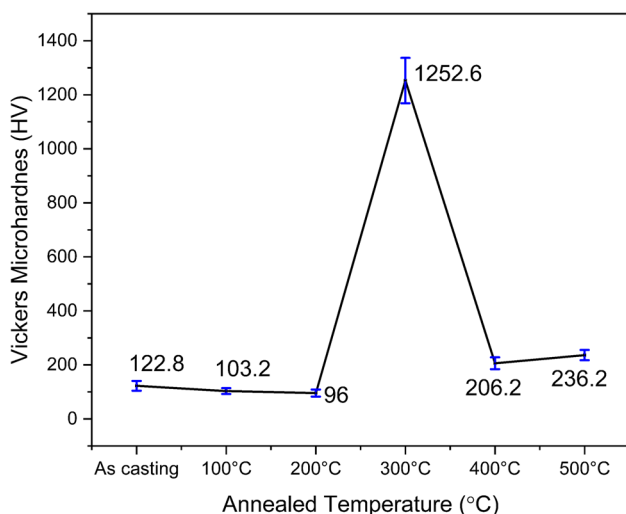are examined, it is thought that a brittle rupture of the alloy occurs.

Fig. 9 XRD pattern of $Al_{92}Mg_5Ti_2B_1$ alloy produced by normal solidification after heat treatment

Fig. 10 SEM images of $Al_{92}Mg_5Ti_2B_1$ alloy after heat treatment **a** 100 °C, **b** 200 °C, **c** 300 °C, **d** 400 °C, and **d** 500 °C
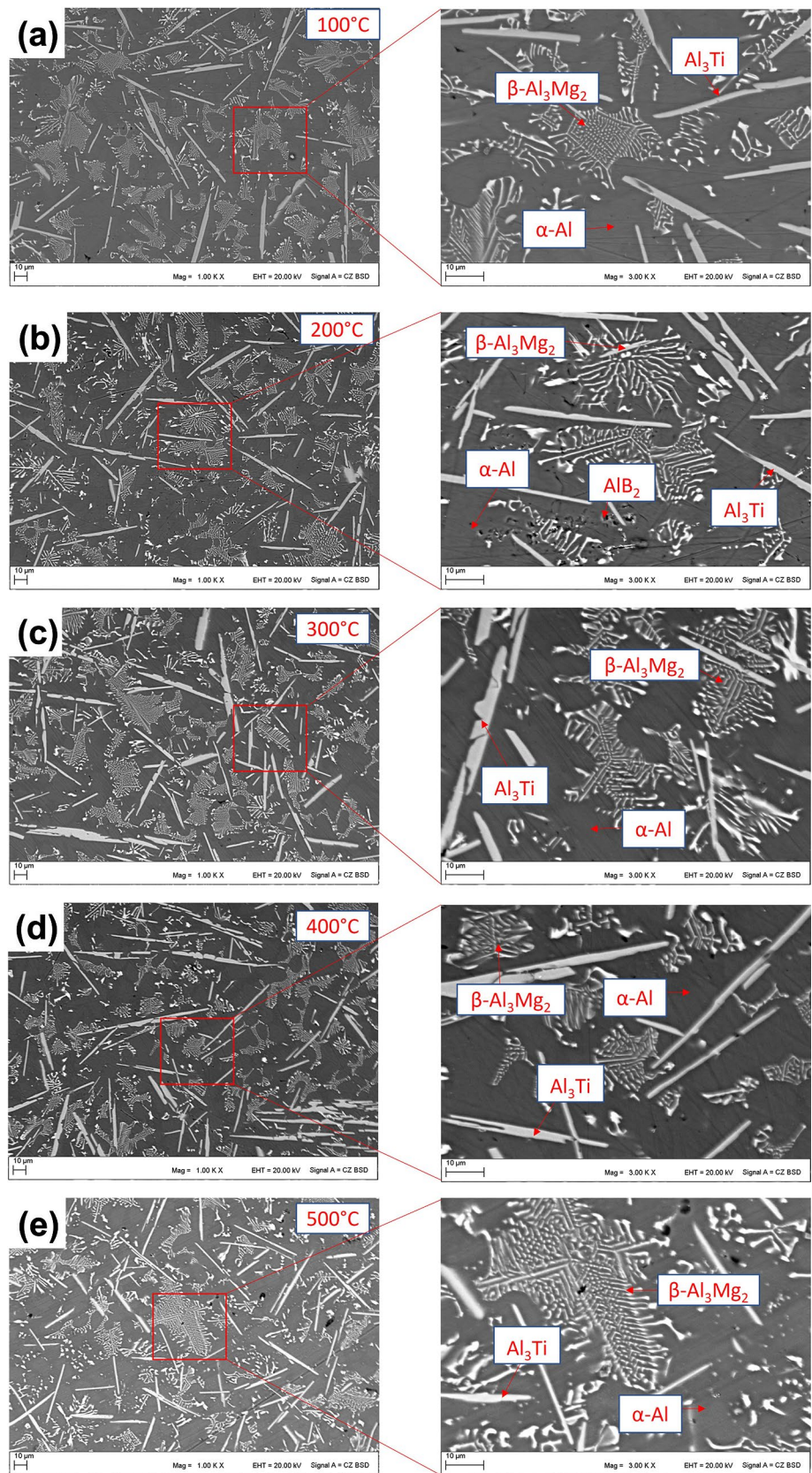
Fig. 11 Vickers microhardness results after annealing of $Al_{92}Mg_5Ti_2B_1$ alloy

Effect of Heat Treatment on Alloys

XRD Analysis

$Al_{92}Mg_5Ti_2B_1$ alloy produced by normal solidification was subjected to heat treatment, and the changes in the microstructure and phases of the alloys as a result of heat treatment were investigated. To alloy, heat treatment was applied at constant temperatures of 100 °C, 200 °C, 300 °C, 400 °C, and 500 °C for 2 hours, and the alloys were left to cool at room temperature after heat treatment. Figure 9 shows XRD graphs of $Al_{92}Mg_5Ti_2B_1$ alloy after heat treatment. As shown in Figure 9, cubic α-Al, hexagonal β-Al_3Mg_2, cubic $Al_{12}Mg_{17}$, tetragonal Al_3Ti, and hexagonal AlB_2 phases were observed in the microstructures after heat treatment. There was no significant change in the phase structure of this alloy after heat treatment. This shows that the current phases are stable. As shown in Figure 9 in the $Al_{92}Mg_5Ti_2B_1$ alloy, the α-Al phase has the most intense reflection peak among these phases.

SEM Analysis

SEM examined microstructures and morphological appearance of $Al_{92}Mg_5Ti_2B_1$ alloy after heat treatment. SEM images of these alloys are given in Figure 10. As seen in the SEM photographs of these alloys, the dark regions represent the α-Al phase. In addition, gray-colored rod-like structures and very few pointy or small fractured structures are seen in these photographs. It was determined by EDS analysis that the rod-like structures belong to the Al_3Ti phase, and the rod-like small fracture structures

belong to the AlB_2 phase. It was determined that the dendritic structure was the β-Al_3Mg_2 phase. After heat treatment, dendritic structures grew, and rod-like structures were determined to shrink. The phases observed in the SEM photographs agree with the XRD results.

Microhardness

Figure 11 shows the microhardness values of $Al_{92}Mg_5Ti_2B_1$ after heat treatment at different temperatures. As shown in Figure 11, after heat treatment at temperatures of 100 °C, 200 °C, 300 °C, 400 °C, and 500 °C are calculated, respectively, as 122.8 HV, 103.2 HV, 96 HV, 1252.6 HV, 206.2 HV, and 236.6 HV the microhardness values of the alloy. Compared to casting alloy results, the microhardness value of the alloy increased 10 times after 2 hours of treatment at 300 °C. The increase in microhardness values after heat treatment is thought to be the shrinkage of the rod-like Al_3Ti phases and the growth of the dendritic β-Al_3Mg_2 phase. In addition, according to the results, it can be seen that the increase in the boron ratio in the alloy increases its microhardness value.

Conclusions

This work aims to produce Al-Mg-Ti-B light alloys with normal solidification techniques and to examine these alloys' structural, thermal, and mechanical properties. Al-Mg-Ti-B alloys have been successfully produced as ingots. It has been determined that all alloys produced with normal solidification techniques have a crystal structure. Microstructures of alloys from XRD analysis results determined that they consisted of α-Al, β-Al_3Mg_2, $Al_{12}Mg_{17}$, Al_3Ti, and AlB_2 phases. In the SEM images of the alloys, the phases in the morphological structures of the alloys were determined. From these phases, It was determined that the dark-colored base is the α-Al phase, the rod-like structures are the Al_3Ti phase, the gray-colored structure is the β-Al_3Mg_2 phase, and the point-like small fracture structures are the AlB_2 phase. Phases identified by SEM images were confirmed by EDS analysis. By XRF analysis, it was determined that the compositions of the alloys were homogeneous and similar in initial ratios. In the DSC analysis of all alloys, an endothermic peak was observed only at 660 °C, representing aluminum's melting temperature. Microhardness values of alloys: calculated between 122.8 ± 5 HV and 207 HV. The hardness values of the alloys increased with the increase in the boron and titanium ratio. All alloys' highest tensile strength value was calculated as 169.03 MPa in $Al_{92}Mg_5Ti_2B_1$ alloy.

Declarations

Conflict of interest The authors declare that no known direct or potential conflicts of interest will affect the publication of this paper.

References

1. S. Ji, W. Yang, F. Gao, D. Watson, Z. Fan, Effect of iron on the microstructure and mechanical property of Al-Mg-Si-Mn and Al-Mg-Si diecast alloys. Mater. Sci. Eng. A. **564**, 130–139 (2013). https://doi.org/10.1016/j.msea.2012.11.095

2. M. Vlach, J. Čížek, V. Kodetová, T. Kekule, F. Lukáč, M. Cieslar, H. Kudrnová, L. Bajtošová, M. Leibner, P. Harcuba, J. Málek, V. Neubert, Annealing effects in cast commercial aluminium Al–Mg–Zn–Cu(–Sc–Zr) alloys. Met. Mater. Int. (2019). https://doi.org/10.1007/s12540-019-00499-6

3. S. Das, N.S. Lim, H.W. Kim, C.G. Park, Effects of heat treatment on microstructure and mechanical properties of twin roll cast Al-5.5Mg-0.02Ti alloy. Mater. Des. **31**, 3111–3115 (2010). https://doi.org/10.1016/j.matdes.2009.12.039

4. Y. Sui, Q. Wang, G. Wang, T. Liu, Effects of Sr content on the microstructure and mechanical properties of cast Al-12Si-4Cu-2Ni-0.8Mg alloys. J. Alloys Compd. **622**, 572–579 (2015). https://doi.org/10.1016/j.jallcom.2014.10.148

5. O. Prach, O. Trudonoshyn, P. Randelzhofer, D. Körner, K., Effect of Zr, Cr and Sc on the Al–Mg–Si–Mn high-pressure die casting alloys. Mater. Sci. Eng. A. **759**, 603–612 (2019). https://doi.org/10.1016/j.msea.2019.05.038

6. H. Alizadeh Razazi, M. Paidar, O.O. Ojo, Effect of Mn and Cr on structure and mechanical properties of Al-10%Mg-0.1%Ti alloy. Vacuum. **155**, 619–630 (2018). https://doi.org/10.1016/j.vacuum.2018.06.071

7. Y. Jia, S. Wang, D. Shu, Grain size prediction and investigation of 7055 aluminum alloy inoculated by Al–5Ti–1B master alloy. J. Alloys Compd. **821**, 153504 (2020). https://doi.org/10.1016/j.jallcom.2019.153504

8. L. Lu, M.O. Lai, Y.H. Toh, L. Froyen, Structure and properties of Mg-Al-Ti-B alloys synthesized via mechanical alloying. Mater. Sci. Eng. A. **334**, 163–172 (2002). https://doi.org/10.1016/S0921-5093(01)01790-7

9. C. Gras, M. Meredith, J.D. Hunt, Microdefects formation during the twin-roll casting of Al-Mg-Mn aluminium alloys. J. Mater. Process. Technol. **167**, 62–72 (2005). https://doi.org/10.1016/j.jmatprotec.2004.09.084

10. B. Li, Q. Pan, C. Chen, H. Wu, Z. Yin, Effects of solution treatment on microstructural and mechanical properties of Al-Zn-Mg alloy by microalloying with Sc and Zr. J. Alloys Compd. **664**, 553–564 (2016). https://doi.org/10.1016/j.jallcom.2016.01.016

11. Q. Zhang, B.L. Xiao, Z.Y. Ma, In situ formation of various intermetallic particles in Al-Ti-X(Cu, Mg) systems during friction stir processing. Intermetallics. **40**, 36–44 (2013). https://doi.org/10.1016/j.intermet.2013.04.003

12. Y.H. Cai, C. Wang, J.S. Zhang, Microstructural characteristics and aging response of Zn-containing Al-Mg-Si-Cu alloy. Int. J. Miner. Metall. Mater. **20**, 659–664 (2013). https://doi.org/10.1007/s12613-013-0780-x

13. H.C. Jiang, L.Y. Ye, X.M. Zhang, G. Gu, P. Zhang, Y.L. Wu, Intermetallic phase evolution of 5059 aluminum alloy during homogenization. Trans. Nonferrous Met. Soc. China English Ed. **23**, 3553–3560 (2013). https://doi.org/10.1016/S1003-6326(13)62900-3

14. Z. Hu, L. Wan, S. Wu, H. Wu, X. Liu, Microstructure and mechanical properties of high strength die-casting Al-Mg-Si-Mn alloy. Mater. Des. **46**, 451–456 (2013). https://doi.org/10.1016/j.matdes.2012.10.020

15. I.V. Povstugar, A.N. Streletskii, D.G. Permenov, I.V. Kolbanev, S.N. Mudretsova, Mechanochemical synthesis of activated Me-BN (Me{double bond, long}Al, Mg, Ti) nanocomposites. J. Alloys Compd. **483**, 298–301 (2009). https://doi.org/10.1016/j.jallcom.2008.07.185

16. Lumley, R. (2010) Fundamentals of aluminium metallurgy: production, processing and applications. Elsevier

17. T. Tański, P. Snopiński, K. Prusik, M. Sroka, The effects of room temperature ECAP and subsequent aging on the structure and properties of the Al-3%Mg aluminium alloy. Mater Charact. **133**, 185–195 (2017). https://doi.org/10.1016/j.matchar.2017.09.039

18. Y. Zhang, X. Huang, Z. Ma, Y. Li, F. Guo, J. Yang, Y. Ma, Y. Hao, The influences of Al content on the microstructure and mechanical properties of as-cast Mg-6Zn magnesium alloys. Mater. Sci. Eng. A. **686**, 93–101 (2017). https://doi.org/10.1016/j.msea.2016.12.122

19. L.P. Bu, Y. Gao, G.L. Li, W.D. Zhang, X.H. De, Effect of B2O3 on microstructures and mechanical properties of cast Mg-Al-Ti-B alloys. Trans. Nonferrous Met. Soc. China English Ed. **23**, 2260–2264 (2013). https://doi.org/10.1016/S1003-6326(13)62726-0

20. Y. Huashun, J.D. Kim, S.B. Kang, The formation of AlN and TiN particles during nitrogen bearing gas injection into Al-Mg-Ti melt. Mater. Sci. Eng. A. **386**, 318–325 (2004). https://doi.org/10.1016/j.msea.2004.07.049

21. Khaliq, A., Rhamdhani, M.A., Brooks, G.A., Grandfield, J. (2014) Analysis of boron treatment for V removal using AlB 2 and AlB 12 based master alloys

22. H.K. Yang, J. Qiu, C. Cao, Y.D. Li, Z.X. Song, W.J. Liu, Theoretical design and experimental study of the interlayer of Al/Mg bimetallic composite plate by solid-liquid cast rolling. Mater. Sci. Eng. A. **835**, 142677 (2022). https://doi.org/10.1016/j.msea.2022.142677

23. M. Zeren, E. Karakulak, Influence of Ti addition on the microstructure and hardness properties of near-eutectic Al-Si alloys. J. Alloys Compd. **450**, 255–259 (2008). https://doi.org/10.1016/j.jallcom.2006.10.131

24. F. Wang, D. Eskin, T. Connolley, J. Mi, Effect of ultrasonic melt treatment on the refinement of primary Al3Ti intermetallic in an Al-0.4Ti alloy. J. Cryst. Growth. **435**, 24–30 (2016). https://doi.org/10.1016/j.jcrysgro.2015.11.034

25. X.-G. An, Y. Liu, J.-W. Ye, L.-Z. Wang, P.-Y. Wang, Grain refining efficiency of SHS Al–Ti–B–C master alloy for pure Aluminum and its effect on mechanical properties. Acta Metall. Sin. English Lett. **29**, 742–747 (2016). https://doi.org/10.1007/s40195-016-0452-8

26. G.K. Sigworth, The grain refining of Aluminum and phase relationships in the Al-Ti-B system. Metall. Trans. A. **15**, 277–282 (1984). https://doi.org/10.1007/BF02645112

27. H. Eskalen, S. Uruş, H. Yaykaşlı, M. Gögebakan, Microstructural characterization of ball milled Co 60 Fe 18 Ti 18 Nb 4 alloys and their photocatalytic performance. Alloy Mater. Their Allied Appl. (2020). https://doi.org/10.1002/9781119654919.ch6

28. M. Gogebakan, B. Avar, Quasicrystalline phase formation during heat treatment in mechanically alloyed Al65Cu20Fe15 alloy. Mater. Sci. Technol. **26**, 920–924 (2010)

29. B. Avar, T. Simsek, S. Ozcan, A.K. Chattopadhyay, B. Kalkan, Structural stability of mechanically alloyed amorphous (FeCoNi)70Ti10B20 under high-temperature and high-pressure. J. Alloys Compd. **860**, 158528 (2021). https://doi.org/10.1016/j.jallcom.2020.158528

30. Y. Chen, W. Cao, S. Li, C. Chen, J. Xie, Microstructure and mechanical properties of friction stir weld of dissimilar Ti6Al4V titanium alloy to AA2024 Aluminum alloy. Trans. Intell. Weld. Manuf. **1**, 153–162 (2018). https://doi.org/10.1007/978-981-10-7043-3_11

31. K.A. El-Aziz, E.M. Ahmed, A.H. Alghtani, B.F. Felemban, H.T. Ali, M. Megahed, D. Saber, Development of Al–Mg–Si alloy performance by addition of grain refiner Al–5Ti–1B alloy. Sci. Prog. **104**, 1–15 (2021). https://doi.org/10.1177/00368504211029469

32. L. Bolzoni, N. Hari Babu, On the grain refining efficacy of Ti-free hypoeutectic AlSi via AlTiB AlB and AlNbB chemical inoculation. J. Alloys Compd. (2020). https://doi.org/10.1016/j.jallcom.2019.152807

33. S. Zhou, Z. Zhang, M. Li, D. Pan, H. Su, X. Du, P. Li, Y. Wu, Correlative characterization of primary particles formed in as-cast Al-Mg alloy containing a high level of Sc. Mater Charact. **118**, 85–91 (2016). https://doi.org/10.1016/j.matchar.2016.05.011